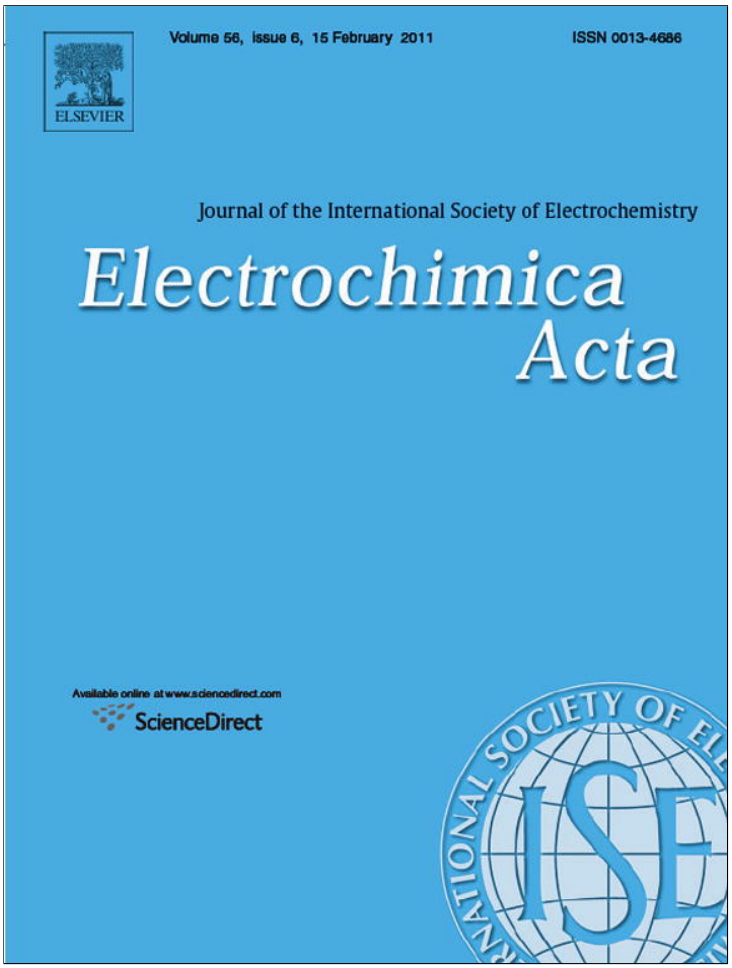

Electrochimica Acta 56 (2011) 2648–2655

Contents lists available at ScienceDirect

Electrochimica Acta

journal homepage: www.elsevier.com/locate/electacta

Mn influence on the electrochemical behaviour of $Li_3V_2(PO_4)_3$ cathode material

Marcella Bini, Stefania Ferrari, Doretta Capsoni*, Vincenzo Massarotti

Department of Physical Chemistry "M. Rolla", University of Pavia, Viale Taramelli 16, 27100 Pavia, Italy

ARTICLE INFO

Article history:
Received 6 July 2010
Received in revised form 6 December 2010
Accepted 6 December 2010
Available online 16 December 2010

Keywords:
$Li_3V_2(PO_4)_3$
Mn substitution
Cyclic voltammetry
XRPD
Cathode material

ABSTRACT

The role played by the substitution of Mn on the electrochemical behaviour of $Li_3V_2(PO_4)_3$ has been investigated. Independently of the synthesis route, the Mn doping improves the electrochemical features with respect to the undoped samples. Different reasons can be taken into consideration to explain the electrochemical enhancement. In the sol–gel synthesis the capacity slightly enhances due to the Mn substitution on both the V sites, within the solubility limit $x = 0.124$ in $Li_3V_{2-x}Mn_x(PO_4)_3$. In the solid state synthesis the significant capacity enhancement is preferentially due to the microstructural features of the crystallites and to the $LiMnPO_4$ phase formation.

1. Introduction

The research on cathode materials for lithium rechargeable batteries is now very active due to the high demand of power sources with low environmental impact [1,2]. Besides the well known $LiCoO_2$, $LiNiO_2$ and $LiMn_2O_4$ [3,4], the lithium metal phosphates are promising compounds due to their high intercalation voltage (about 4 V depending on the material) and long life cycling and stability [5–7]. Among the phosphates, the olivine type materials are widely investigated [8–11] but, at present, compounds with NASICON structure are emerging. In particular, $Li_3V_2(PO_4)_3$ is attracting much interest due to its high theoretical capacity (197 mAh/g) and its thermal stability [12] that make it suitable for high power density and large scale applications. However, as for the major part of the compounds belonging to this class of materials, the low electronic conductivity and cyclability limit their wide application. In order to overcome these restrictions, different synthesis routes, such as sol–gel, solid state, carbothermal reduction and hydrothermal synthesis, were developed to obtain an ideal particle morphology and a proper carbon coating, both necessary to favour the intercalation/deintercalation process [13–18].

The substitution of vanadium with other transition metal ions e.g. Fe, Co, Cr, Ti, Zr [19–23] or with non electrochemically active elements such as Mg and Al [12,24] has also been investigated as an alternative way to enhance the cycling stability and rate performance of this material. $Li_3V_2(PO_4)_3$ can exist in the monoclinic or rhombohedral structure and in the high temperature orthorhombic γ-phase. The room temperature (RT) monoclinic structure (space group $P2_1/n$) displays two V crystallographic sites, V1 and V2. Both sites have the highest multiplicity (4e site) for this space group. A slightly distorted octahedron is centred on both sites.

It has been proved that the doping does not cause structural changes except for the Zr substitution which stabilizes the orthorhombic γ-phase [23] characterized by a better ionic conductivity than the monoclinic one at RT.

The aim of the present article is to investigate the effect of Mn doping on the structure and electrochemical properties of $Li_3V_{2-x}Mn_x(PO_4)_3$.

Both sol–gel ($0 \le x \le 0.30$) and solid state ($0 \le x \le 0.20$) synthesis routes have been employed for the preparation of the samples. Each sample has been electrochemically characterized by cyclic voltammetry and charge–discharge measurements. The electrochemical features have been related to the structure and microstructure-morphology, investigated by the structural refinement (Rietveld method) of X-ray powder diffraction (XRPD) data, by scanning electron microscopy (SEM) measurements and by Raman spectroscopy.

2. Experimental

The $Li_3V_{2-x}Mn_x(PO_4)_3$ samples were synthesized via both solid state and sol–gel syntheses.

The sol–gel samples with $x = 0.0$, 0.10, 0.20 and 0.30 (SG, SG10, SG20 and SG30 in the following) were prepared by using the procedure reported in the literature [14], and adding Mn_2O_3 (Aldrich, 99.999%) in the proper amount to obtain the desired stoichiometry for the doped samples. Citric acid (Aldrich, 99+%) was used as

* Corresponding author. Tel.: +39 382 987213; fax: +39 382 987575.
E-mail address: capsoni@unipv.it (D. Capsoni).

0013-4686/$ – see front matter © 2010 Elsevier Ltd. All rights reserved.
doi:10.1016/j.electacta.2010.12.011

chelating agent and source of carbon. Each sample was treated 8 h at 750 °C and 8 h at 800 °C in N_2 flow, with intermediate grinding.

Two samples with $x = 0.0$ and 0.20 (SS and SS20 respectively) were also prepared by solid state synthesis using the carbothermal reduction method [25,26] from stoichiometric amount of Li_2CO_3 (Aldrich, 99.6%), V_2O_5 (Aldrich, 99.6%), $(NH_4)_2HPO_4$ (Merck, 99%) and Mn_2O_3; carbon black (Alfa) was added to reduce the vanadium ions to the 3+ oxidation state (1 wt% C excess with respect to the stoichiometric amount). The mixtures were ball milled in tungsten carbide jars for 30 min at 400 rpm; in particular the jar containing the SS20 mixture was hermetically closed in Ar to prevent the oxidation during the milling processes. The thermal treatment was performed in N_2 flow at 300 °C for 4 h and at 900 °C for 16 h.

RT XRPD measurements were performed in air on a Bruker D5005 diffractometer with the CuKα radiation, Ni filter and a position sensitive detector (PSD). Rietveld structural and profile refinement was carried out by means of TOPAS V3.0 program [27].

The SEM measurements were performed with a Zeiss EVO®-MA10-HR microscope on Au sputtered samples.

Micro-Raman measurements were carried out at RT by using a Labram Dilor spectrometer equipped with an Olympus microscope HS BX40. The 632.8 nm light from He–Ne laser was employed as excitation radiation. The samples, mounted on a motorized xy stage, were tested with a 100× objective and with a laser spot of about 1 mm of diameter. The spectral resolution was about 1 cm^{-1}.

An ICP-OES Perkin Elmer Optima 3300 DV was used for the elemental analysis measurements, following the operating conditions suggested by the manufacturers.

Conductivity measurements (IS) were carried out by means of Autolab PGSTAT30 in the frequency range 10^5–1 Hz. IS measurements were performed as a function of temperature on disk shaped samples sintered at the final synthesis temperatures of SS20 and SG20 samples, covered with Ag to deposit the electrodes and inserted in a polythermal electrochemical cell.

In order to prepare the cathode layer, a slurry was made by mixing the $Li_3V_{2-x}Mn_x(PO_4)_3$ active material with carbon black (Alfa) and poly(vinylidene fluoride) (PVdF, Solvay) in N-methyl-2-pyrrolidone (NMP, Aldrich) with a weight ratio of 75:15:10. The obtained suspensions were spread on an aluminium current collector by using a doctor blade. After the evaporation of the solvent in an oven at 60 °C for 24 h, the foils were transferred to an Ar-filled dry-box (MBraun, <1 ppm O_2, <1 ppm H_2O). They were cut into disks of 1 cm diameter with a loading of about 4 mg/cm^2 of active material; considering their surface, thickness and the low mass loading, an average error of about 4% on the reversible capacity can be estimated (the significant digits are related to this error). The electrochemical tests were performed using a three-electrodes T-cell with lithium metal as the negative electrode and a glass-wool (Whatman GF/A) disc as the separator. The electrolyte was 1 M $LiPF_6$ in ethylene carbonate/diethyl carbonate (EC/DEC) 1:1 (Merck). All the cells were assembled in a dry-box under Argon atmosphere. The cyclic voltammetry (CV) was performed by using a Solartron Electrochemical Interface 1287 at a scan rate of 0.1 mV/s in the potential range 3.0–4.8 V. All the cells were tested at room temperature. The galvanostatic cycling tests were carried out using the same apparatus between 3.0 and 4.8 V. The cells were charged and discharged at C/10.

3. Results and discussion

Fig. 1a and b shows the XRPD patterns of the sol–gel and solid-state samples respectively. The peaks are explained on the basis of the $Li_3V_2(PO_4)_3$ monoclinic structure. No impurity phases are present in the SS sample, while small amounts of Li_3PO_4 (+), $LiMnPO_4$ (*) or both are observed in the other ones.

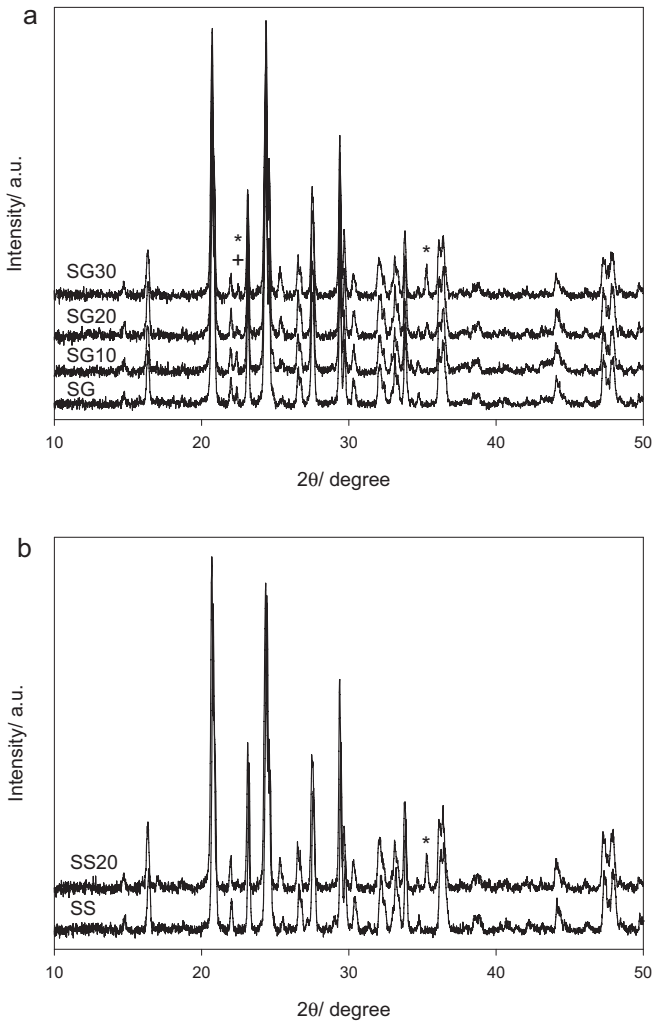

Fig. 1. XRPD patterns of a) sol–gel and b) solid state samples. The Li_3PO_4 (+) and $LiMnPO_4$ (*) impurity phases are also indicated.

The structural and profile refinement on the basis of the Rietveld method was performed on the XRPD patterns of all the samples. The lattice parameters, the cell volume, the isotropic thermal factors B (constrained for the same ion type) [28], and the impurity phases wt% obtained by the refinement are reported in Table 1. The discrepancy factors and goodness of fit are also shown. Their values indicate satisfactory results for the refinement procedure, as also demonstrated in Fig. 2 by the comparison of the calculated and experimental patterns for the SG20 sample, taken as an example.

Reliable values for the B factors are obtained from the refinement. For what concerns the lithium sites, B values of about 4 $Å^2$ and 2 $Å^2$ are found for the sol–gel and solid state samples respectively. These values are not surprising for this ion, in particular for the Li^+ penta-coordinated to oxygen ions. No trend is observed on both lattice parameters and cell volume by increasing x; this is expected on the basis of the similar values of the ionic radii of Mn^{2+} and V^{3+} ions in octahedral coordination [29]. EPR measurements performed on SG10 sample suggest the +2 oxidation state for the Mn ion; no Mn^{3+} has been detected. This result is consistent with the carbothermal reduction synthesis. Interesting considerations regarding the synthesis route and the Mn amount effectively substituted in the $Li_3V_2(PO_4)_3$ structure can be performed by analysing the impurity phases percentages obtained by the refinement. Li_3PO_4 forms only from the sol–gel route and, for the doped samples, its abundance decreases by increasing x and it is not detected for the

Table 1
Thermal factors (B), lattice parameters, cell volume, impurity phases, abundance (wt%) and discrepancy factors (R_{wp} and GoF) obtained by Rietveld structural refinement on the investigated samples.

	SG	SG10	SG20	SG30	SS	SS20
B(Li)/Å^2	4.2(9)	4.9(11)	4.4(9)	3.5(10)	2.0(8)	1.6(8)
B(V)/Å^2	0.63(4)	0.77(5)	0.86(5)	0.83(5)	0.29(4)	0.29(5)
B(P)/Å^2	0.82(8)	0.68(9)	0.66(7)	0.67(9)	0.40(8)	0.63(8)
B(O)/Å^2	1.48(9)	1.60(11)	1.42(9)	1.50(11)	1.89(10)	1.07(10)
a/Å	8.6076(2)	8.6056(3)	8.6058(2)	8.6082(3)	8.5993(3)	8.6014(3)
b/Å	8.5931(2)	8.5969(3)	8.5956(2)	8.5959(3)	8.5993(3)	8.5947(3)
c/Å	12.0382(3)	12.0419(4)	12.0411(3)	12.0404(4)	12.0384(4)	12.0388(4)
β/°	90.574(2)	90.560(2)	90.567(2)	90.558(2)	90.542(2)	90.557(2)
V/Å^3	890.38(5)	890.83(6)	890.66(4)	890.89(6)	890.18(5)	889.94(5)
wt%Li_3PO_4	2.9(2)	5.6(3)	1.4(2)	–	–	–
wt%$LiMnPO_4$	–	–	2.9(1)	8.1(2)	–	7.8(2)
R_{wp}	4.85	4.55	4.05	3.67	4.54	4.23
GoF	1.27	1.28	1.20	1.14	1.25	1.18

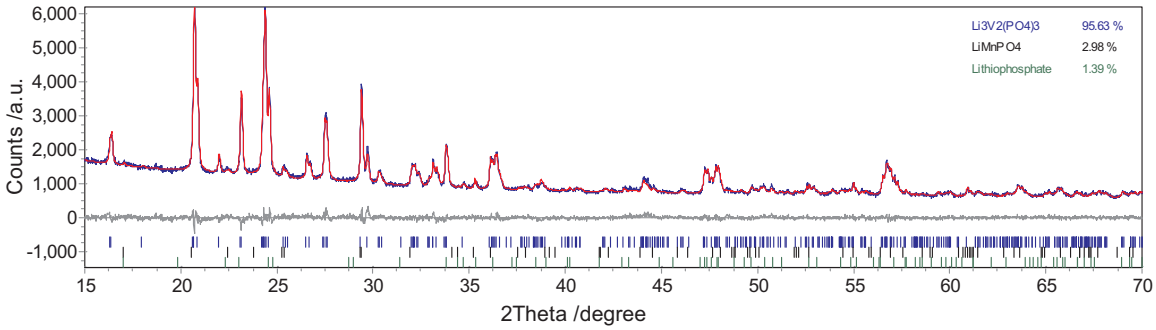

Fig. 2. Comparison between the observed (blue line) and calculated (red line) pattern obtained after the Rietveld refinement for SG20 sample. In the bottom, the difference curve (gray line) and the peak positions (bars) are also shown. (For interpretation of the references to colour in this figure legend, the reader is referred to the web version of this article.)

$x = 0.30$ sample, for which, instead, the highest amount of $LiMnPO_4$ is observed. This phase is also present in the SS20 in an amount of 7.8 wt%, higher than that obtained for the same Mn doping by sol–gel synthesis (SG20). The segregation of the $LiMnPO_4$ impurity phase suggests that a solubility limit is reached by increasing the x value and only for the SG10 sample the Mn substitution on V sites is effective. Moreover for the same nominal composition ($x = 0.20$) a different Mn insertion into the $Li_3V_2(PO_4)_3$ structure, depending on the synthetic route, is obtained. The $LiMnPO_4$ wt% (Table 1) and the total Mn amount used in the synthesis can be used to estimate the effective Mn quantity substituted in the $Li_3V_2(PO_4)_3$ structure. The calculated values are reported in Table 2. The cation content was also evaluated by elemental analysis with ICP on the SS20 and SG20 samples obtaining the molar ratios: V/Li = 0.62 and Mn/Li = 0.071 for SS20 and V/Li = 0.65 and Mn/Li = 0.070 for SG20 ([Mn]/[Mn + V] = 0.103 for SS20 and 0.0972 for SG20), in good accordance with the values expected from the synthesis stoichiometry (V/Li = 0.60 and Mn/Li = 0.067; [Mn]/[Mn + V] = 0.100). These results indicate that no lithium loss have occurred during the synthesis. These ratios can be calculated also by the weight percentage and the stoichiometry of the phases obtained by the Rietveld refinement; V/Li = 0.62 and Mn/Li = 0.068 for SS20, V/Li = 0.58 and Mn/Li = 0.063 for SG20 were found ([Mn]/[Mn + V] = 0.0988 for SS20 and 0.0979 for SG20). A 4% for SS20 and 0.7% for SG20 of discrepancy between ICP and Rietveld results is found, so indicating a good agreement between the two techniques. In Table 2 the results of the refinement of the Mn content on the two vanadium crystallographic sites are also reported: Mn distributes on both sites, with a preference for the V1 one. The maximum value of Mn substitution is obtained for the SG20 sample and $x = 0.124$ can be considered the limit composition of our solid solution. In the SS20 sample all the Mn amount used in the synthesis forms $LiMnPO_4$ and only a low Mn substitution (below the detection limit of our technique) is obtained, notwithstanding the higher sintering temperature (900 °C and 800 °C for solid state and sol–gel samples respectively). So, only the sol–gel synthesis seems to be effective, within a solubility limit, for the Mn substitution.

Table 2
Effective Mn content and its distribution on the vanadium sites (V1: $x = 0.25103$, $y = 0.45935$, $z = 0.10936$; V2: $x = 0.75307$, $y = 0.47451$, $z = 0.39038$ in fractional coordinates) obtained by the Rietveld refinement.

	Mn amount in $Li_3V_2(PO_4)_3$	Mn on V1 site	Mn on V2 site
SG10	0.10	0.056(4)	0.044(4)
SG20	0.124	0.065(4)	0.059(4)
SG30	0.089	0.076(5)	0.013(5)
SS20	0.000	–	–

The effect of sintering on the particle size and morphology is put into evidence by SEM investigations. The micrographs reported in Figs. 3 and 4 show significant differences between the SS and the SG samples. The SS and SS20 samples (Fig. 3) are characterized by very large aggregates (tens and hundreds of μm) of rounded particles (about 5 μm), but strictly linked together by partially fused parts and, especially for the SS20 sample, covered by fine particles (Fig. 3b and d). Hence, the Mn doping seems to play a favourable role on the formation of well separated crystallites covered by small particles (Fig. 3d). The peculiar shape and dimension of the SS20 particles could favour the formation of a thin and homogeneous carbon layer coated on $Li_3V_2(PO_4)_3$. The micro-Raman spectroscopy gives additional information about the carbon coating of solid state and sol–gel samples. As an example, the spectra obtained on SS20 and SG20 samples, representatives of each synthesis route, are shown in Fig. 5. In both the samples the broad D and G bands of carbon, peaked at about 1320 cm^{-1} and 1600 cm^{-1}, are detected [30,31]. The G line is associated with the optically allowed E_{2g} zone center mode of crystalline graphite, and the D line is associated with

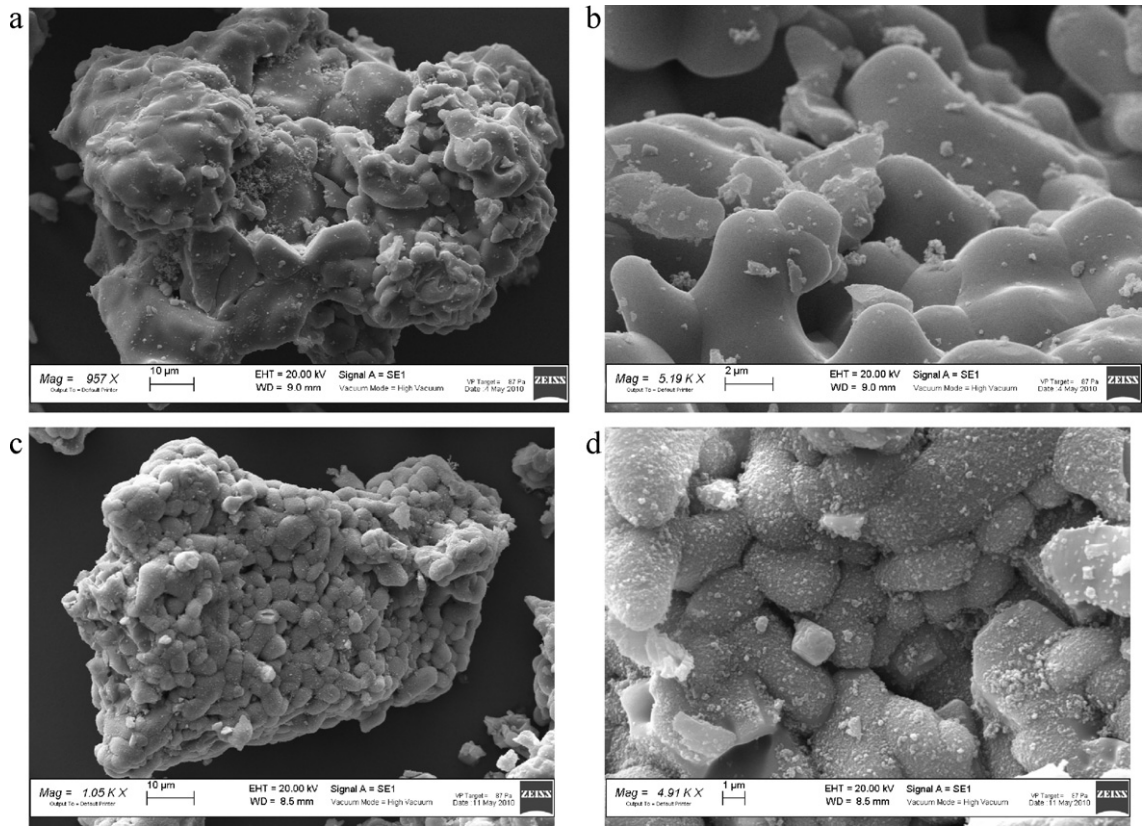

Fig. 3. SEM micrographs of solid state samples: (a and b) SS; (c and d) SS20.

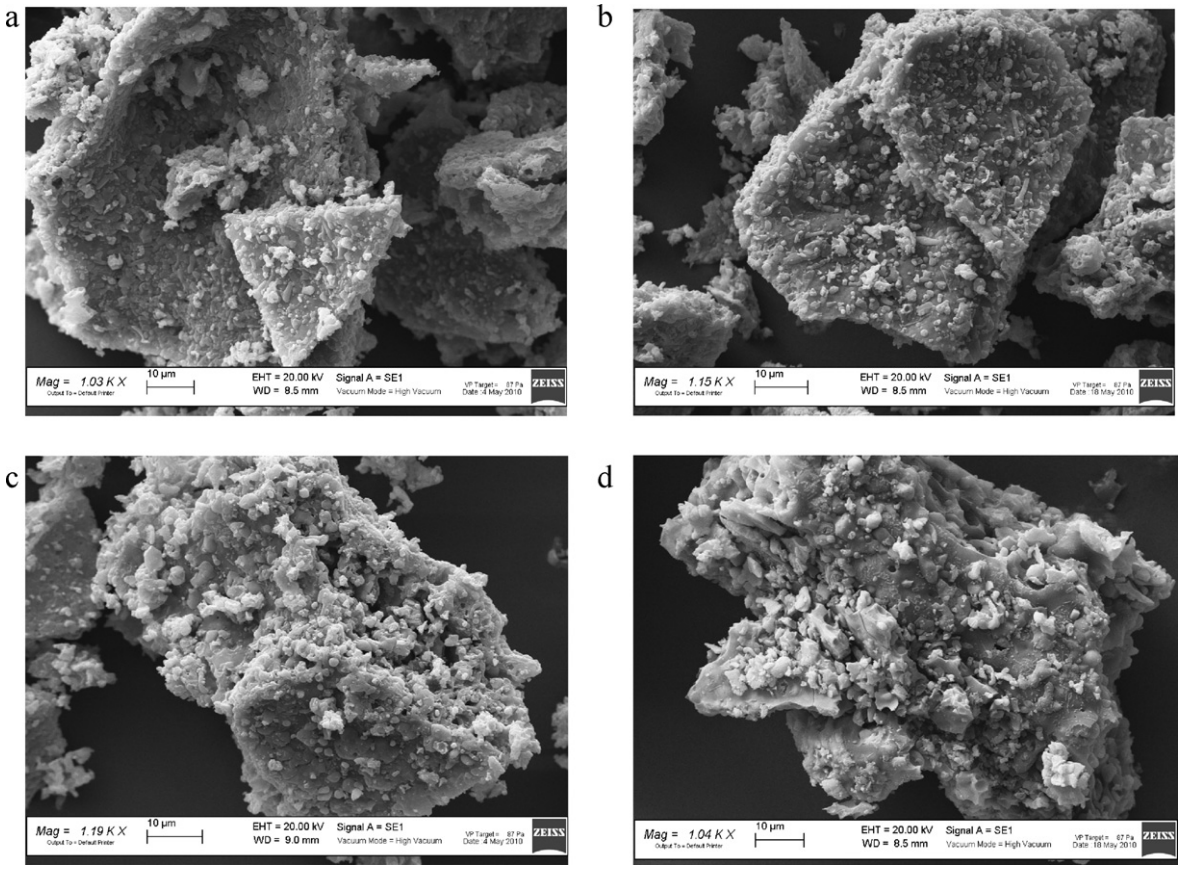

Fig. 4. SEM micrographs of sol–gel samples: a) SG, b) SG10, c) SG20 and d) SG30.

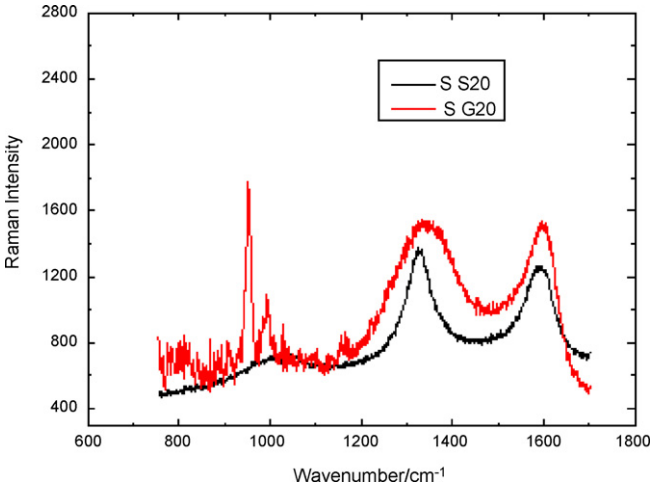

Fig. 5. Micro Raman spectra of SG20 and SS20 samples.

disorder-allowed zone-edge modes of graphite. These broadened spectral features indicate that a highly amorphous carbon film is deposited on both the samples. Only for the SG20 sample, two additional peaks in the 900–1050 cm^{-1} spectral region are observed; these features can be attributed to the vibrational modes of the PO_4^{3-} units. The occurrence of these peaks indicates a less homogeneous and uniform carbon coating of the $Li_3V_2(PO_4)_3$ particles in the SG20 with respect to the SS20 sample. The microstructure and homogeneous carbon layer peculiar of the SS20 sample could facilitate the electronic transfer among the $Li_3V_2(PO_4)_3$ particles, possibly affecting positively the capacity. A clear indication of this benefit comes from the electric conductivity measurements; in fact, the conductivity values obtained for the SS20 sample are slightly higher than those of the SG20 one (Fig. 6). The SG and SG10 samples (Fig. 4) also show particle agglomerates whose dimension are close to that of the solid state samples, and covered by crystallites of about 1 μm. For the SG20 and SG30 this effect is less evident. In fact the rounded particles are more separated than in the case of the other sol–gel. For all the samples the presence of wide particles can be likely ascribed to the lithium source (Li_2CO_3 used in both our synthesis procedure) that, as suggested in the literature [32], is known to favour the formation of large crystallites.

The cyclic voltammetry of the first and fourth cycles for sol–gel samples is reported in Fig. 7a and b, respectively. The voltammetry curve shows three oxidation peaks in the potential range of 3.0–4.10 V and a peak at about 4.50 V associated to the last lithium

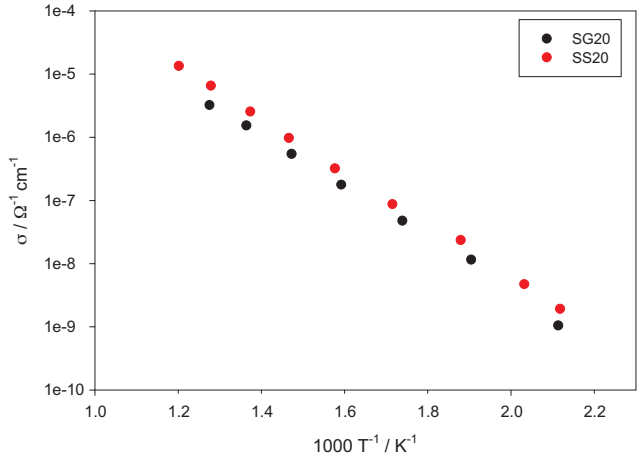

Fig. 6. Arrhenius plot of electric conductivity for SS20 and SG20 samples.

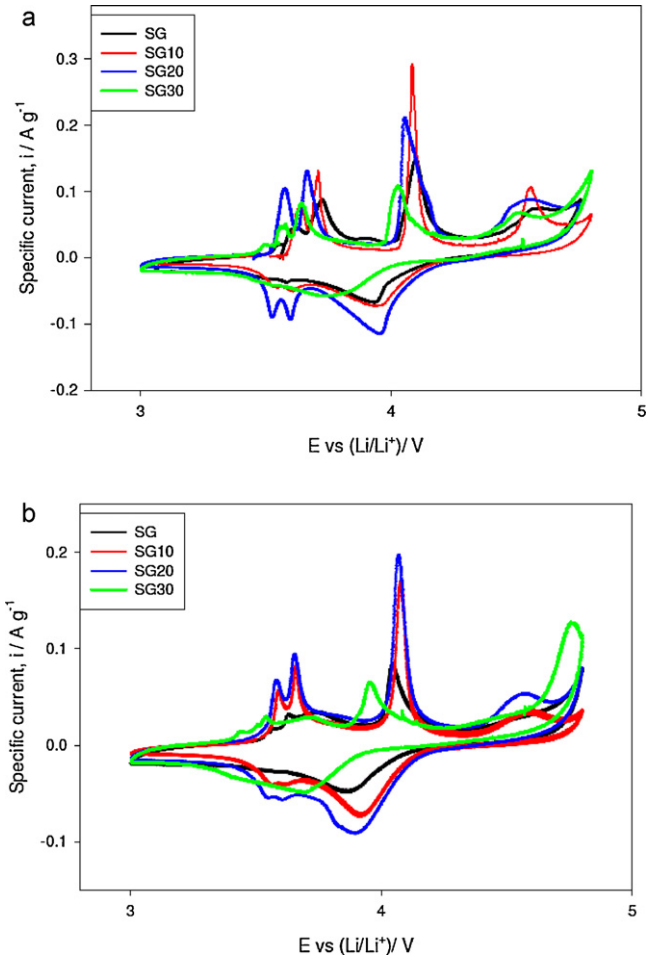

Fig. 7. Cyclic voltammetry of a) the first and b) the fourth cycles of sol–gel samples.

extraction, that is the kinetically most difficult process and leads to the formation of the completely lithium free phase $V_2(PO_4)_3$ [16,19,20]. In particular, the anodic peaks of the first cycle are located at 3.6 V, 3.72 V, 4.09 V and 4.57 V for SG, 3.63 V, 3.7 V, 4.08 V and 4.56 V for SG10, 3.58 V, 3.65 V, 4.05 V and 4.54 V for SG20 and 3.57 V, 3.65 V, 4.03 V and 4.5 V for SG30; a progressive decrease of the anodic peak position is observed by increasing the Mn content. For the SG30 sample, the additional peak at 3.49 V can be likely due to an impurity phase that can intercalate lithium ions and which is probably present in an amount below the detection limit of XRPD technique or whose diffraction peaks are in complete overlapping with those of the main phase. The Mn doping sharpens the peaks, particularly in the case of SG10 sample, which is free of Mn containing impurity phases. For the SG20 and SG30 samples we observe a shoulder at 4.14 V and 4.2 V respectively, likely due to the presence of the electrochemically active $LiMnPO_4$ [33]. In fact, the electrochemically active Mn ion can oxidize ($2+ \rightarrow 3+$): the voltage of this oxidation/reduction in the olivine-like structures (lithiofilite) is about 4.2/3.9 V [33], very close to that of the V^{3+}/V^{4+} couple. The voltage value for Mn oxidation/reduction is therefore in significant overlapping with that of vanadium ion, and, during the first cycle, a shoulder in the voltage anodic signal can be appreciated.

In the cathodic part of the voltammetry the sharpening effect increases with increasing the Mn amount up to $x = 0.20$. In particular, the peaks at 3.6 and 3.52 V suggest that the insertion process in the SG20 sample is more ordered than for the other samples. This behaviour has been also evidenced for Co, Cr and Fe doped $Li_3V_2(PO_4)_3$ samples [19–21]. On the contrary, the SG and SG30

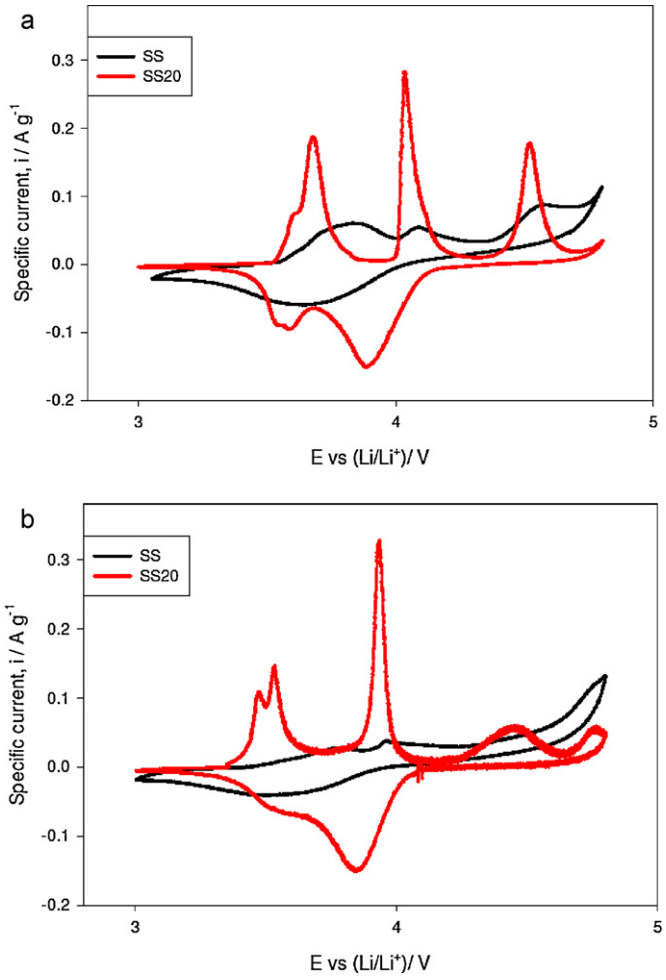

Fig. 8. Cyclic voltammetry of a) the first and b) the fourth cycles of solid state samples.

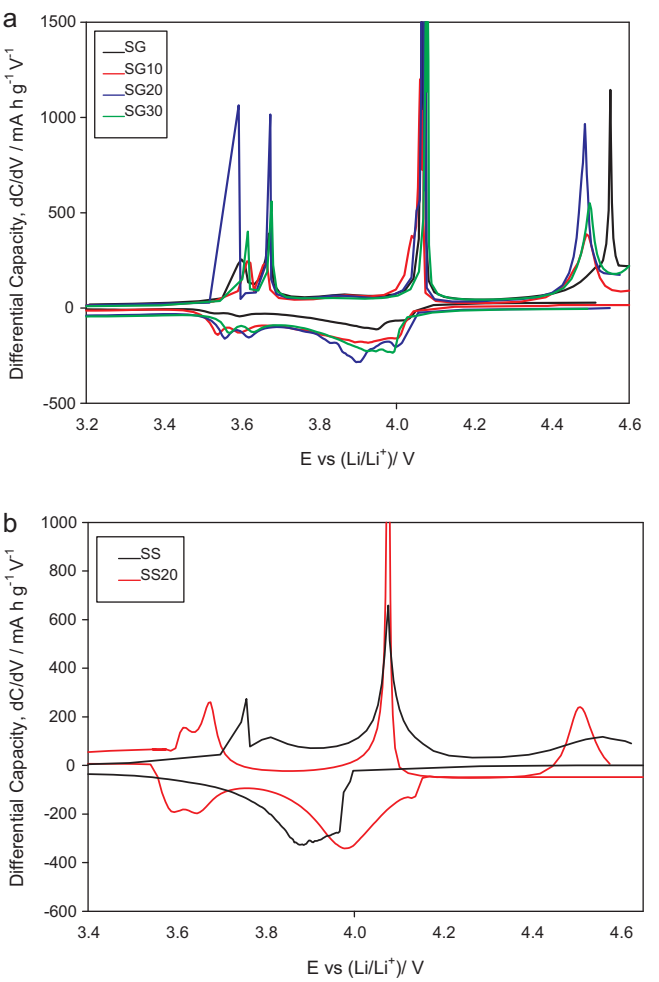

Fig. 9. Differential capacity curve of a) sol–gel and b) solid state samples.

samples show very weak and not distinguishable cathodic peaks at about 3.58 and 3.49 V. These experimental evidences can be supported by the morphological features of the samples (Fig. 4). In fact, the SG20 sample shows rounded separated particles, in contrast to the SG one characterized by wide particle agglomerates. The small and separated crystals allow to obtain a more efficient extraction of lithium and electrons, thus playing a favourable role on the electrochemical behaviour of the sample [32].

In the fourth cycle (Fig. 7b) the intensity of the peaks in the range 3.5–3.7 V decreases for SG sample, suggesting that the lithium extraction process becomes irreversible. This effect is not present for the doped samples up to $x = 0.20$; the peaks position and intensity completely overlap and the insertion and extraction processes remain reversible.

In Fig. 8a and b the CV curves of first and fourth cycles for the solid state samples are shown. The anodic peaks are located at about 3.8 V, 4.08 V and 4.57 V for SS and 3.6 V, 3.67 V, 4.03 V and 4.52 V for SS20. The last anodic peak is well defined in SS20 sample suggesting the reversible character of the fourth extraction process notwithstanding its difficult kinetic. A similar behaviour is observed for SG10 sample. We have also to take into account that the Mn substitution for SS20 sample is not effective in accordance with our Rietveld refinement (Table 2). The SS sample in both the first and the fourth cycles presents clear irreversible intercalation/deintercalation processes related to a lithium disorder within the structure [12]. On the contrary, the SS20 sample shows well defined peaks (anodic part of the CV); this feature is maintained also in the fourth cycle except for the last lithium extraction peak at 4.5 V. The position of this peak shifts from 4.52 to 4.43 V and its intensity decreases dramatically. In Fig. 9a and b the differential capacity curves derived by the data of charge/discharge at C/20, second cycle, are shown to better evidence the complex insertion–extraction reactions of the Li ions for all the samples. The main features of the CV plots (Figs. 7 and 8) are confirmed; the Li insertion process is more appreciable, even though broad peaks are observed thus confirming that the associated phenomenon is disordered. For the sol–gel samples, the doping causes a peak shift towards lower voltage, in particular for the peak at about 4.6 V, associated to the last extraction process. This suggests a favourable Mn effect on the electrochemical features of the material, allowing the usage of this phosphate at lower charge voltage as already reported in the literature, in the case of the Al substitution [12].

In the charge–discharge profile (Fig. 10a) of the SS20, four plateaus are present. This sample has a capacity value of about 150 mAh/g in charge and 140 mAh/g in discharge. The SS sample presents a very low value of charge and discharge capacity (about 80 mAh/g and 64 mAh/g, respectively) confirming its disordered structure and in accordance with the CV plot. The two samples, notwithstanding the common synthesis route, show different degrees of particles aggregation (Fig. 3). For what concern the sol–gel samples (Fig. 10b), they show a very similar charge–discharge profile, differently from the solid state ones. In this case the Mn doping is effective and a slight increase of the capacity value is recorded for both the SG10 and SG20 samples with

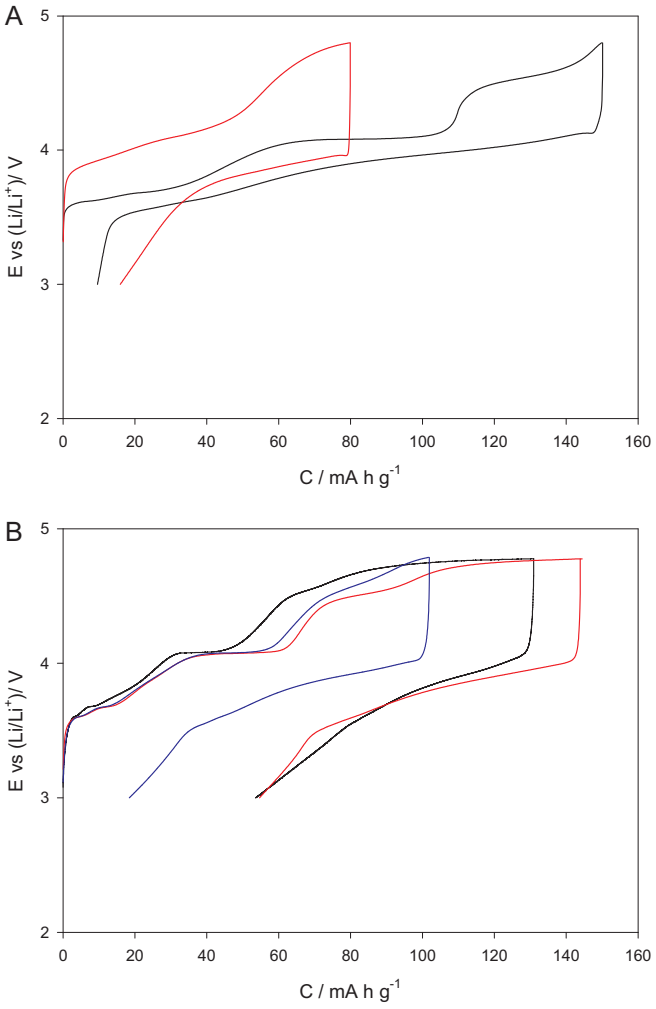

Fig. 10. Charge–discharge at the fourth cycle at C/10 for a) SS (black line) and SS20 (red line) and b) SG (black line), SG10 (red line) and SG20 (blue line). (For interpretation of the references to colour in this figure legend, the reader is referred to the web version of this article.)

respect to the undoped. In addition, a large irreversible capacity for the SG and SG10 samples is evident. In fact, the peaks regarding the last insertion (see Figs. 7 and 9a) are broad in the case of these two samples with respect to the SG20, which seems to possess a less disordered intercalation behaviour. For all of the samples a significant overvoltage between the charge and the discharge curves is evident and it can be ascribed to the high energetics involved in removing the third lithium ion, associated with the redox couple V^{4+}/V^{5+}.

Our results put into evidence that the Mn addition improves the electrochemical features of $Li_3V_2(PO_4)_3$ cathode material, even though different reasons have to be taken into account to explain this enhancement, depending on the synthesis route. In the sol–gel synthesis Mn distributes on both the vanadium sites reaching its solubility limit ($x = 0.124$) in the SG20 sample. So, the Mn substitution is responsible for the electrochemical improvement with respect to the undoped SG sample, as also observed for other transition metals doping [19–21].

More satisfactory electrochemical results and improvement with respect to the undoped SS sample are obtained for the SS20 one: the Mn present in the solid state synthesis forms the $LiMnPO_4$ phase and a very low Mn amount on the V sites of the $Li_3V_2(PO_4)_3$ structure is present. It should be underlined that the sample shows significant morphological differences with respect to the SS and the sol–gel samples, and the optimization of particle size is necessary to improve the electrochemical performances of this material. In addition, a possible $Li_3V_2(PO_4)_3/LiMnPO_4$ composite can be obtained by solid state synthesis and this occurrence could be responsible for the formation of the peculiar morphology observed in the SS20 sample, that plays a favourable role on the electrochemical features. The positive influence of coatings and composites formation in the preparation of electrode materials is currently reported in the literature [34,35].

4. Conclusions

The Mn substitution in $Li_3V_2(PO_4)_3$ compound has been investigated on a series of samples obtained by different synthesis methods.

A solubility limit ($x = 0.124$) is determined for the samples prepared via sol–gel route. The Mn insertion in the cationic framework of $Li_3V_2(PO_4)_3$ plays a favourable role on the electrochemical performances, as demonstrated by the charge–discharge data showing better values with respect to the sol–gel undoped sample.

The solid state synthesis, performed at higher temperature than that of the sol–gel one, favours the preferential formation of $LiMnPO_4$ impurity phase and no Mn seems to substitute V ions in the $Li_3V_2(PO_4)_3$ compounds, as demonstrated by the Rietveld structural refinement on XRPD data. In this case the improvement of the electrochemical performance with respect to the undoped SS sample, being comparable the homogeneous carbon coating, revealed by Raman measurements, can be likely played by the different degrees of particle aggregation of the samples, and by $LiMnPO_4$ segregation.

Acknowledgements

The authors kindly thank Dr. Michela Sturini for the ICP analysis and Dr. Pietro Galinetto for the micro-Raman measurements.

References

[1] M. Armand, J.M. Tarascon, Nature 451 (2008) 652.
[2] D. Aurbach, B. Markovsky, G. Salitra, E. Markevich, Y. Talyossef, M. Coltypin, L. Nazar, B. Ellis, D. Koovacheva, J. Power Sources 165 (2007) 491.
[3] J.W. Fergus, J. Power Sources 195 (2010) 939.
[4] D. Capsoni, M. Bini, G. Chiodelli, V. Massarotti, C.B. Azzoni, M.C. Mozzati, A. Comin, Phys. Chem. Chem. Phys. 3 (2001) 2162.
[5] M.S. Whittingham, Y. Song, S. Lutta, P.Y. Zavalij, N.A. Chernova, J. Mater. Chem. 15 (2005) 3362.
[6] L. Sebastian, J. Gopalakrishnan, J. Mater. Chem. 13 (2003) 433.
[7] A.D. Robertson, A.R. West, A.G. Ritchie, Solid State Ionics 104 (1997) 1.
[8] N. Meethong, Y.H. Kao, S.A. Speakman, Y.M. Chiang, Adv. Funct. Mater. 19 (2009) 1060.
[9] M. Thackeray, Nat. Mater. 1 (2002) 81.
[10] P. Gibot, M. Casas-Cabanas, L. Laffont, S. Levasseur, P. Carlach, S. Hamelet, J.M. Tarascon, C. Masquelier, Nat. Mater. 7 (2008) 741.
[11] M. Bini, M.C. Mozzati, P. Galinetto, D. Capsoni, S. Ferrari, M.S. Grandi, V. Massarotti, J. Solid State Chem. 182 (2009) 1972.
[12] J. Barker, R.K.B. Gover, P. Burns, A. Brayan, J. Electrochem. Soc. 154 (2007) A307.
[13] C. Chang, J. Xiang, X. Shi, X. Han, L. Yuan, J. Sun, Electrochim. Acta 54 (2008) 623.
[14] Y. Li, Z. Zhou, X. Gao, J. Yan, Electrochim. Acta 52 (2007) 4922.
[15] M.M. Ren, Z. Zhou, X.P. Gao, W.X. Peng, J.P. Wei, J. Phys. Chem. C 112 (2008) 5689.
[16] M.Y. Saidi, J. Barker, H. Huang, J.L. Swoyer, G. Adamson, J. Power Sources 119–121 (2003) 266.
[17] T. Jiang, C. Wang, G. Chen, H. Chen, Y. Wie, X. Li, Solid State Ionics 180 (2009) 708.
[18] Y. Li, X. Liu, J. Yan, Electrochim. Acta 53 (2007) 474.
[19] M. Ren, Z. Zhou, Y. Li, X.P. Gao, J. Yan, J. Power Sources 162 (2006) 1357.
[20] Q. Kuang, Y. Zhao, X. An, J. Liu, Y. Dong, L. Chen, Electrochim. Acta 55 (2010) 1575.
[21] S. Zhong, B. Zhao, Y. Li, Y. Liu, J. Liu, F. Li, J. Wuhan Univ. Technol. 24 (2009) 343.
[22] D. Morgan, G. Ceder, M.Y. Saidi, J. Barker, J. Swoyer, H. Huang, G. Adamson, J. Power Sources 119–121 (2003) 755.

[23] M. Sato, H. Ohkawa, K. Yoshida, M. Saito, K. Uematsu, K. Toda, Solid State Ionics 135 (2000) 137.
[24] C. Dai, Z. Chen, H. Jin, X. Hu, J. Power Sources 195 (2010) 5775.
[25] J. Barker, M.Y. Saidi, J.L. Swoyer, J. Electrochem. Soc. 150 (2003) A1267.
[26] J. Barker, M.Y. Saidi, J.L. Swoyer, J. Electrochem. Soc. Solid State Lett. 6 (2003) A53.
[27] Bruker AXS, TOPAS V3.0: General Profile and Structural Analysis Software for Powder Diffraction Data. User Manual, Bruker AXS, Karlsruhe, Germany, 2005.
[28] S.C. Yin, P.S. Strobel, H. Grondey, L.F. Nazar, Chem. Mater. 16 (2004) 1456.
[29] R.D. Shannon, Acta Crystallogr. A 32 (1976) 751.
[30] C.M. Julien, K. Zaghib, A. Mauger, M. Massot, A. Ait-Salah, M. Selmane, F. Gendron, J. Appl. Phys. 100 (2006) 063511.
[31] M. Bini, M.C. Mozzati, P. Galinetto, D. Capsoni, S. Ferrari, M.S. Grandi, V. Massarotti, J. Solid State Chem. 182 (2009) 1972.
[32] P. Fu, Y. Zhao, Y. Dong, X. An, G. Shan, Electrochim. Acta 52 (2006) 1003.
[33] Z. Bakenov, I. Taniguchi, Electrochem. Commun. 12 (2010) 75.
[34] L. Zhang, X.L. Wang, J.Y. Xiang, J. Zhou, S.J. Shi, J.P. Tu, J. Power Sources 195 (2010) 5057.
[35] J.-C. Zheng, X.-H. Li, Z.-X. Wang, S.-S. Niu, D.-R. Liu, L. Wu, L.-J. Li, J.-H. Li, H.-J. Guo, J. Power Sources 195 (2010) 2935.